Finding a better fit for lithium ion batteries: A simple, novel, load dependent, modified equivalent circuit model and parameterization method

Hua, X., Zhang, C. & Offer, G.

Finding a better fit for lithium ion batteries: a simple, novel, load dependent, modified equivalent circuit model and parameterization method

Xiao Hua, [a] Cheng Zhang, [a, c] Gregory Offer [a, b*]

Affiliations:

a.   **Department of Mechanical Engineering, Imperial College London, SW7 2AZ, United Kingdom**

b.   **The Faraday Institution, Harwell Science and Innovation Campus, Didcot, United Kingdom**

c.   **Institute for Future Transport and Cities, Coventry University, CV1 5FB, United Kingdom**

Abstract

Equivalent circuit models (ECM) of lithium ion batteries are used in many applications because of their ease of implementation and low complexity. The accuracy of an ECM is critical to the functionality and usefulness of the battery management system (BMS). The ECM accuracy depends on the parametrization method, and therefore different experimental techniques and model parameter identification methods (PIM) have been widely studied. Yet, how to account for significant changes in time constants between operation under load and during relaxation has not been resolved. In this work a novel PIM and modified ECM is presented that increases accuracy by 77.4% during drive cycle validation and 87.6% during constant current load validation for a large format lithium iron phosphate prismatic cell. The modified ECM uses switching RC network values for each phase, which is significant for this cell and particularly at low state-of-charge for all lithium ion batteries. Different characterisation tests and the corresponding experimental data have been trained together across a complete State-of-Charge (SoC) and temperature range, which enables a smooth transition between identified parameters. Ultimately, the model created using parameters captured by the proposed PIM shows an improved model accuracy in comparison with conventional PIM techniques.

Keywords: Lithium-ion battery, equivalent circuit model parameterization, parameter identification method, lithium iron phosphate, electric vehicle, stationary energy storage.

1. Introduction

Electrification is inevitable. The transformation from internal combustion engine (ICE) transportation to electric drive is dramatically increasing in recent years, due to aggressive policies worldwide driven by air quality, greenhouse emissions and national economic competition. Between 2030-40, a significant majority of countries and/or cities will ban the sales of ICE passenger vehicles, including China, USA, Germany, UK and many more. [1,2] As a consequence the sales of EVs have been increasing dramatically. There are over 2 million electric vehicles sold in 2018, up from just a few thousand in 2010. Bloomberg NEF forecasted that the sales of annual passenger EV will rise to 10 million in 2025, 28 million in 2030 and 56 million by 2040. [3] During this global transport industry paradigm shift, the lithium-ion battery plays a central role in the majority of EVs. [3]

While researching and developing lithium-ion batteries with new materials and manufacturing [4,5], the usage of a robust battery model is pivotal at the application level. Models enable the battery management system (BMS) to improve battery performance and prolong lifetime. [6] There are predominantly three types of models in the literature, which are data-driven models, physics-based models and equivalent circuit models (ECM) [7]. Data-driven models, such as neural networks [8] and support vector machine [9], etc., do not require a physical interpretation of the battery's internal dynamics, making it suitable for simulating complex or unknown systems. However, the model training usually relies on a large amount of data. Further, it is difficult to predict the model's generalization performance under different operating conditions. The test data collection can be time-consuming, and the model training involves complex optimization. The physics-based models capture the physical behaviours through solving equations such as lithium diffusion equations and charge conservation equations. Newman, Doyle, Fuller et al established the foundations for these physics-based model [10,11]. Later, other electrochemical models have been proposed to describe different battery properties, such as capacity fade and electrode particle geometry etc. [12–18]. The main two drawbacks of physics-based models for BMS applications are 1. High complexity of parameterisation; 2. High computational power. There are more than 30 parameters needed to be fitted and parameterised including salt concentration, electrode/separator thickness, conductivity of electrolyte etc. Quite often the parameters in the physics-

based model require ex-situ experimental measurements which are time/cost inefficient. [19,20] Also, the computational speed is another disadvantage of this type of models. Further, it is challenging to scale such model into multi-dimensional or pack level analysis. [16,21,22] Although these drawbacks can be mitigated through reduced order models (ROMs) ECMs are still the model of choice for many applications.

ECMs describe the battery terminal voltage-current dynamics using passive electrical components (resistors and capacitors) and measured/parameterised look-up tables or simple mathematical functions. The ease of implementation and low model complexity make ECM feasible in real-time applications such as integrated BMS systems, and they are regularly embedded in microprocessors and deliver precise simulation/feedback signals in real-time.[23]. The reader is referred to recent reviews by He et al. [24] and Hu et al.[25] on ECM models. A typical ECM consists of the battery open circuit voltage (OCV) and a series ohmic resistor R_0 and several resistor-capacitor (RC) networks [26]. The battery OCV can be measured directly from experimental data using low-rate constant current (CC) (dis)charge (giving a pseudo-OCV), or using a pulsed current (dis)charge with long rest periods between pulses (true OCV) [27]. The RC values, on the other hand, need to be identified by fitting the model's voltage prediction under current load to measurements using optimisation algorithms [28,29]. This represents the model parametrization procedure.

The parameter identification method (PIM) is critical for the ECM model accuracy. The model accuracy is correlated with what and how PIM is used for the certain Li-ion battery. There are various PIMs for ECM parametrization in the literature, including genetic algorithm (GA) [30], particle swarm optimization (PSO) algorithm [31], and the least-squares method [32,33]. A recent study conducted by Lai et al [34] compared 9 different popular PIMs for 9 different ECM models in the entire SoC area and demonstrated the importance of the PIM to the model accuracy.

The ECM parameters depend on the operating conditions. The popular methods for capturing this parameter dependency include offline parameterized look-up tables [35–37] and the online adaptive parameter estimation algorithms such as recursive least squares methods [28,38] and the dual Kalman filter algorithms [39]. Existing PIMs mainly focus on capturing the parameter dependence on the SoC, temperature

and current directions. However, another important dependency factor for ECM parameters that is generally overlooked is the type of current loads. Different current profiles have been used for ECM parameter estimation, such as the pulsed current test (different types of pulse design as in [36,37,40]), drive cycles [41,42] and constant-current charging and discharging [43–45]. However, few works have considered the effect of choosing different current profiles on the identified parameters and the model accuracy [41,42]. The battery is an electrochemical system with complex internal dynamics, and ECM is an approximate reduced-order model. Therefore, different current excitations will reveal different system properties. As a result, the ECM parameters will vary under different load conditions [46,47]. Waag et al [47] analysed the dependency of the ECM parameters on the frequency characteristics of the load current, and proposed an application-specific parametrization method by taking into consideration the frequency spectrum of the load current. However, the switching scheme between different load conditions is not addressed in [47]. Further, because of the nonlinearity of the battery dynamics, it is not straightforward to translate the frequency domain analysis to time-domain implementation. The influence of the load current profile on the ECM parameters was also studied in [42]. However, the study is limited to a few standard drive cycles that are usually used for battery characterization, and the underlying mechanism is not explained.

There is one key difference in the current load that the studies in the literature were missing, which is the difference in the underload and the relaxation. Generally the model parameters were identified without distinguishing the two different working conditions and the underload and relaxation test data are used together for ECM parametrization [36,40]. However, the test data analysis on the chosen cell in this paper shows that the battery performs distinctly differently during underload and relaxation, in terms of the scale of magnitude of time constants of the RC networks. It shows that using the same parameter set cannot capture both the underload and the relaxation dynamics accurately. Therefore, this paper proposes a parameter switching scheme between underload and relaxation working conditions to address this problem.

Further, this study delivers a novel PIM that captures ECM parameter dependence on load switching, SoC (0-100%) and temperatures ($10°C$, $20°C$, $30°C$ and $40°C$). The novelty of the proposed PIM is that the time constants of the RC networks are independent from SoC and temperature. The rest parameters, i.e., the resistor values,

then become linear-in-the-variable which can be readily obtained using computationally efficient least squares optimization solvers. This also enables the simultaneous estimation of all the resistor values under all SoC and temperatures levels with parameter constraints to ensure a smooth transition between different temperature levels. In theory, the battery internal resistance is reversely proportional with the operating temperature. However, in the conventional way of parameter identification, the resistance values might zig-zag across a range of temperatures without using parameter constraints [29]. The ultimate purpose of this novelty is to provide a temperature dependent ECM model e.g. [21], in many BMS and modelling applications, which is critical for the model accuracy. This proposed PIM shows a better fit for large current/large power/large heat generation applications. Unlike smaller cells, large format cells have significant heat generation challenges, therefore training the data within the operating temperature window is important and inevitable.

The rest of the paper is structured as follows. The ECM equations are expressed in Section 2. The experimental design for battery characterization and model validation is introduced in Section 3. Then, in Section 4 there is a detailed data analysis and the introduction of the novelties of the proposed PIM. In Section 5, the modelling results are validated against the experimental data from Section 3. Also, there is one comparative study between the proposed PIM and conventional method. Please note, in the main paper there are only experimental data and its corresponding validation results under a single thermal chamber temperature. The rest results at other temperature levels can be found in the supplementary material A. Lastly, Section 6 concludes this study.

2. ECM Equations

The typical n-th order battery ECM consists of n RC networks connected in series with the OCV and internal resistor R_0. The OCV represents the equilibrium voltage, and R_0 captures the total ohmic resistance of the current collectors, electrode and electrolyte. The battery's internal polarization overpotential is captured by the RC networks, which have different time constants to represent the battery internal dynamics at different timescales, such as the slow diffusion and fast charge transfer.

Let v, i represent the battery terminal voltage and current, respectively. Denote n_{rc} as the number of RC networks and define v_j, i_j, $j = 1,2,\ldots,n_{rc}$ as the voltage and current through R_j. Then, $v_j = R_j i_j$. Let $\tau_j = R_j C_j$ be the time constant. Then

$$i_j(k+1) = a_j i_j(k) + (1 - a_j)i(k), \quad j = 1,2,\ldots,n_{rc} \tag{1}$$

where

$$a_j = exp(-T_s/\tau_j)$$

$i_j(k)$ stands for i_j at the k-th sampling time, and T_s is the sampling interval (s).

The battery SoC is obtained using the widely employed coulomb counting method [29,36],

$$SoC(k+1) = SoC(k) + \frac{T_s}{3600C_n} i(k) \tag{2}$$

where C_n is the battery nominal capacity at $25°C$ (unit: Ampere-hour). Next, the battery terminal voltage can be expressed as,

$$v(k) = OCV(k) + R_0 i(k) + \sum_{j=1}^{n_{rc}} R_j i_j(k) \tag{3}$$

3. Experimental details

This section introduces the detailed experimental procedure of the battery characterisation, and the test data are used for identifying the OCV, R_0 and RC values. The OCV hysteresis effect is not considered in this paper, therefore only experimental data for discharge current was used for parameter training and validation. The data sampling rate is 1Hz under current load and during relaxation periods.

The battery is always charged using the same constant current constant voltage (CC-CV) test procedure to make sure the initial SoC of the battery is consistent between tests. The CC current is 1C (90A) and the CV voltage is 3.65V. The cut-off charging current of CV procedure is C/50 (1.8A). The cut-off voltage during discharge procedure is 2.5V.

A range of pulse discharge characterisation tests, on a high capacity 90Ah Lithium iron phosphate (LFP) cathode based, graphite anode battery with aluminium/prismatic shell (200.5 x 130.3 x 36.5 mm) were examined under various temperatures. Before

characterisation tests were carried out, the cell underwent five 1C (90A) charge/discharge cycles for pre-conditioning and demonstrated stabilised capacity. After the pulse discharge characterisation tests, a range of validation tests were examined, including drive cycle discharge with noisy current load at $20°C$ and constant current discharge under various temperatures. The cell was evenly wrapped with nitrite rubber insulation material (RS Pro, thickness 25 mm, thermal conductivity 0.034 W/mK) across entire cell surface, as shown in the figure 1. The cell was placed in the centre of the bottom shelf of a thermal chamber (Binder, model KB23). The thermal boundary condition has been designed in this format to approach a near 'adiabatic condition' by minimizing convection in the thermal chamber, this is done to minimize the internal thermal gradient of the cell being tested and to avoid the problems this can cause as described by Zhao et al.[21] The same thermal boundary condition was implemented in the model. K-type thermocouple was placed and taped with Kapton$^®$ polyimide films tape on the centre of the prismatic aluminium shell surface (200.5 x 130.3 mm) to measure surface temperature, as marked in Figure 1. A single channel battery cycling system (BioLogic, HCP-1005) was used for charging/discharging the cell. One set of characterisation pulse discharge tests, one validation noisy load drive cycle test and one set of constant current discharge tests were carried out in this study, as detailed below.
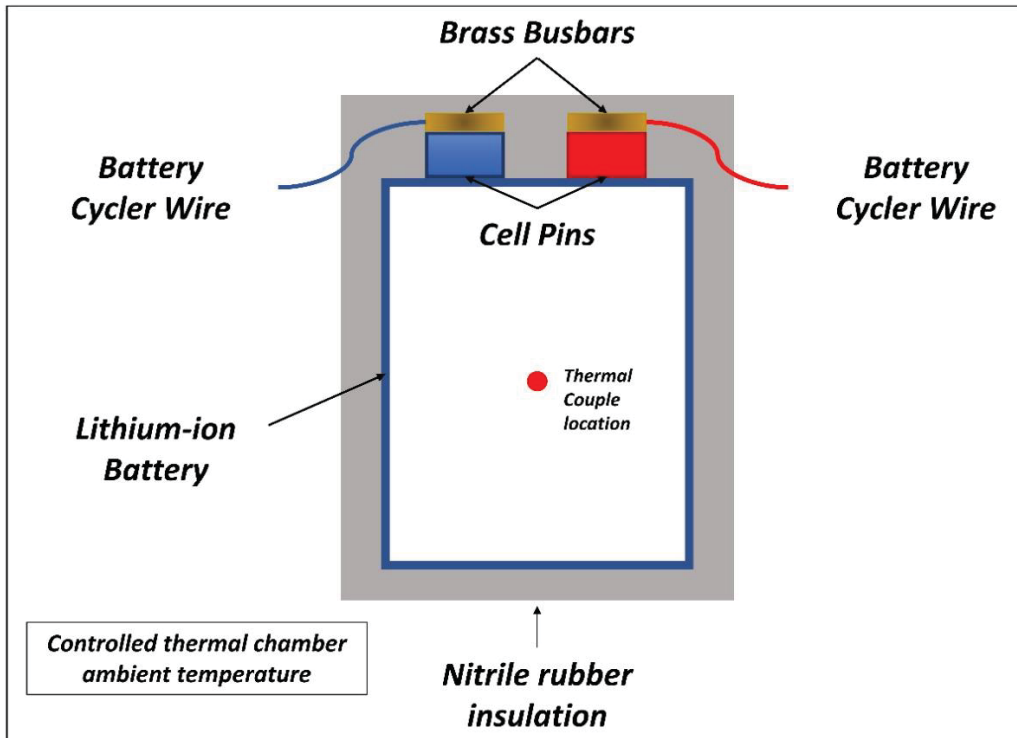
Figure 1 Battery testing rig demonstration

3.1. Experiment #1: variable ambient temperature characterisation pulse discharge tests

Characterisation pulse discharge (PD) tests were carried out to generate data for the PIMs in this work. The measurement involves repetitions of a constant current discharge pulse at 1C (90A) followed by a resting period of 2 hours. This process starts from 100% SoC and finished at 0% SoC. The SoC breakpoints step length is 1% (9Ah) for 0% -10%, 90% - 100% SoC, and 5% (4.5Ah) for 10% - 90%. The current input and the corresponding voltage response are shown in Figure 2. Also, in Figure 2(d), the cell surface centre temperature is presented, where a maximum temperature difference at different SoC is about 0.5 °C. The measurements were repeated for a range of temperatures ($10°C$, $20°C$, $30°C$ and $40°C$). Here, Figure 2 only shows data at $20°C$ as an example, and all the other data can be found in supplementary material A.

Figure 2: Test data for the pulse discharge experiment at 20°C thermal chamber ambient temperature: (a) Input current, (b) Terminal voltage, (c) SoC profile, (d) Measured surface temperature.

3.2. Experiment #2: validation noisy load drive cycle discharge test

The model and the parameters are validated using independent sets of experiment data. The first one is the bespoke designed noisy load discharge which based on the US06 drive cycle current profile with enlarged average current value and extended test time. The Figure 3 demonstrates the current profile examined, the voltage and cell surface temperature responses respectively.
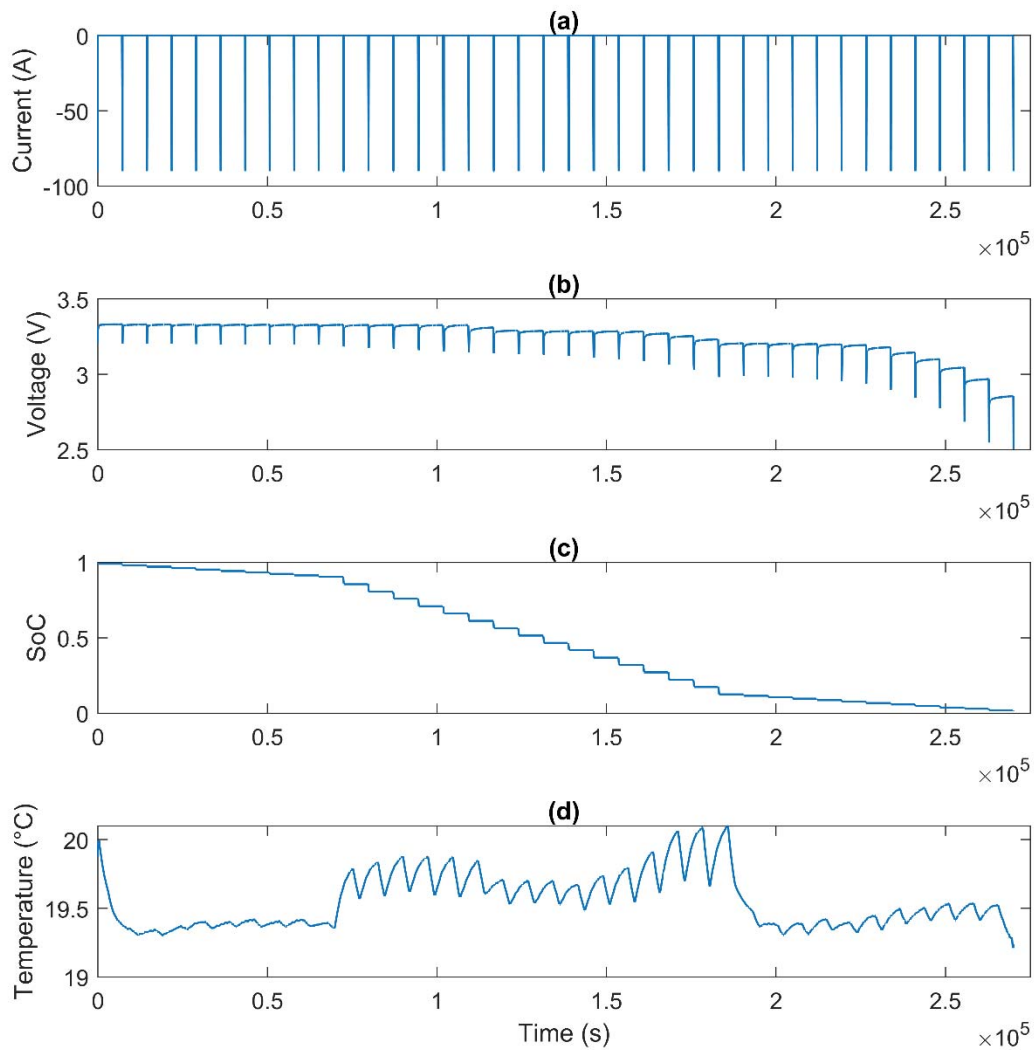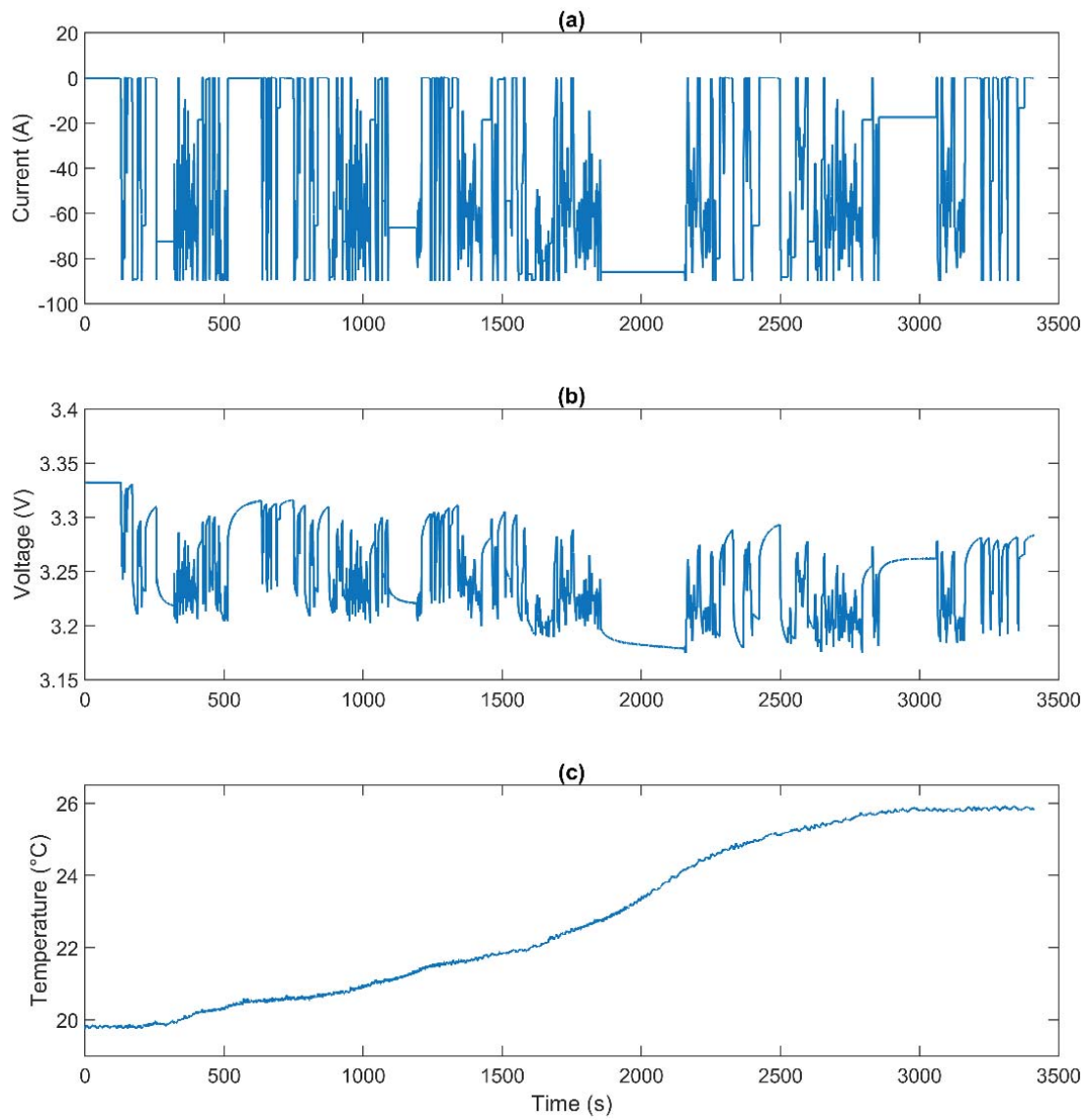
Figure 3: Test data for the discharge drive cycle experiment at 20°C thermal chamber ambient temperature: (a) Input Current, (b) Terminal voltage, (C) Cell centre surface temperature.

3.3. Experiment #3: variable ambient temperature validation constant current discharge tests

The second set of validation experiments are constant current discharge tests. The measurement involves a constant current discharge at 1C (90A). This process starts from 100% SoC and finished when the voltage reaches 2.5V. The current input and the corresponding voltage and cell surface temperature responses are shown in Figure 4. The measurements were repeated for a range of temperatures ($10°C$, $20°C$, $30°C$ and $40°C$). Here, the Figure 4 only shows $20°C$ as an example, and all the other data can be found in supplementary material A.
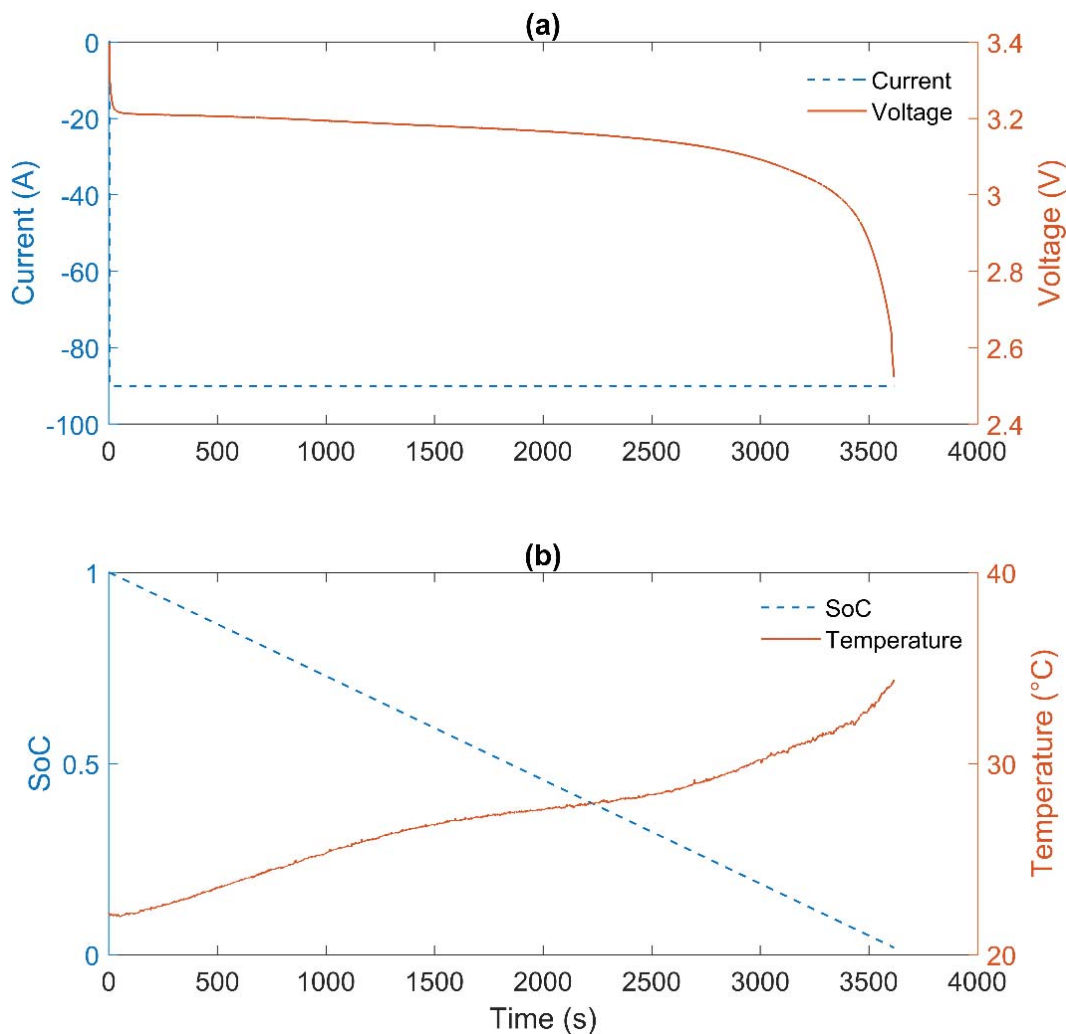

Figure 4: Test data for the constant current discharge experiment at $20°C$ thermal chamber ambient temperature: (a) Input current & terminal voltage, (b) Cell centre surface temperature & SoC profile.

4. Data analysis and ECM parameter estimation

Open circuit voltage measurement

The battery OCV is captured by the pulse discharge test followed by 2 hours rest. The test data is shown in Figure 2. The battery OCV between the SoC breakpoints is calculated with the commonly used linear interpolation method [29,48].

4.1. RC network characterisation

After collecting experimental data, it is essential to conduct a detailed data analysis to better understand the battery properties under study. A single pulse discharge data segment shown in Figure 2 is used here for data analysis. The SoC value decreases from 50% to 45%. A detailed look is presented in the Figure 5a, which shows an underload period of 1C (90A) constant current discharge load for 180 seconds (5% SoC breakpoint step) followed by a 2-hour relaxation period.

Since both the SoC and temperature changes are small for this single pulse discharge (The SoC decreases by 5%, and the battery's surface temperature variation is less than 1℃.), the model parameters are assumed to be constant. There are mature methods in the literature, such as the cross-validation method, for selecting the number of RC networks, which for this study was chosen to be 3 following the procedure described in [36,40]. It is found that 3 RC networks can capture both the underload and relaxation dynamics with high accuracy and 4 RC networks provides negligible accuracy improvement. The ECM RC parameters, including the time constants in Eq (1) and the resistor values in Eq (3), are obtained following an optimization procedure to minimize the root mean square error (RMSE) between the model voltage output and the measurements. The Matlab function 'fmincon' is used for the numerical optimization. This optimization involves only 6 parameters and is a standard procedure and therefore not detailed here.

The results give an indication that it is difficult to capture both the battery underload and relaxation voltage profiles accurately using a single parameter set. This is because large RC time constants are required to capture the 2-hour voltage relaxation, while only small RC time constants are required to capture the underload voltage profile. In this study, the LFP cell has a nominal capacity of 90Ah with a dimension of W200.5 x L130.3 x H36.5 mm. This large-size battery is an energy cell with thick electrodes. It

is therefore hypothesized that the fast electrochemical reactions at the interface between the electrode and the electrolyte dominate the voltage response under load, while the slow diffusion dynamics inside the solid electrode particles dominate the voltage output during relaxation. Therefore, these two working conditions require RC time constants at different magnitudes. This data analysis process leads to the first novelty of this study, which captures the significant time constant difference between under load phase and relaxation phase using a parameter switching scheme, as follows,

$$\tau_j = \begin{cases} \tau_{j,u}, & if \ |i| > i_{th} \\ \tau_{j,r}, & if \ |i| \le i_{th} \end{cases}, j = 1,2,3 \tag{4}$$

where $\tau_{j,u}$ represents the underload time constant and $\tau_{j,r}$ the relaxation time constant. The current threshold value $i_{th} = 0.1A$ is used in this paper.

Note that this switching scheme will not cause sudden jumps of the state variables, as shown in Eq (1). Only the poles of the transfer function of the RC networks vary with parameter-switching, and the gain (the resistor value) is not affected. Further, the parameter-switching is only triggered when the battery switches between underload and relaxation operating conditions, therefore the switching bandwidth is much lower than the model dynamics (around 1Hz) in EV driving conditions.

To illustrate the comparison between the underload and relaxation dynamics, four parameter identification cases are compared. The first case uses only the underload data for parameter identification. The second case uses underload test data and 500-second relaxation period. The third uses the underload with the full 2-hour relaxation data. The fourth case represents the proposed parameter switching scheme.

Table 1 introduces the time constants obtained in these four case studies, and the modelling results are given in Figure 5 which compares the measured data with the simulation results. As it can be seen in Table 1, the time constants grow with the length of the relaxation period used for parameter identification. Using underload data alone for parameter identification in Case 1, the model can capture the underload dynamics with high accuracy. However, the model error during the relaxation period is high. This is because the maximum RC time constant is only 35.7s, which cannot reproduce a 2-hour voltage relaxation profile. The relaxation stage voltage profile can be better captured in Case 2 and 3, however, this comes at a cost of a larger underload

modelling error. This can be clearly seen in Figure 5(b), i.e., the zoomed segment at the end of the pulse discharge, where the model outputs of Case 2 and Case 3 produce an over-shoot error. It can be predicted that if the current pulse is longer, the underload modelling error will further increase. This is because, the three RC networks with high time constants ($\tau_3 = 2285.1s$) and large resistance values are needed in order to sustain the 2-hour voltage relaxation, which compromised the underload accuracy. This shows an apparent trade-off between the quality of fitting for underload region and the relaxation region, regardless of the length of the relaxation data being examined. The underload stage needs small RC time constants, while the relaxation stage needs long RC time constants. By using the proposed switching time constants in Eq (4), the results in Figure 5 (a)&(b) show good model accuracy for both underload and relaxation, which essentially solve this issue. It is noteworthy that not all lithium ion battery cells show such distinctive features between underload and relaxation stages across their full SOC range, but it is often observed at the extremes, particularly at low SOC when state estimation can be particularly important. Therefore, this study highlights the importance of considering the load dependency of the ECM parameters.
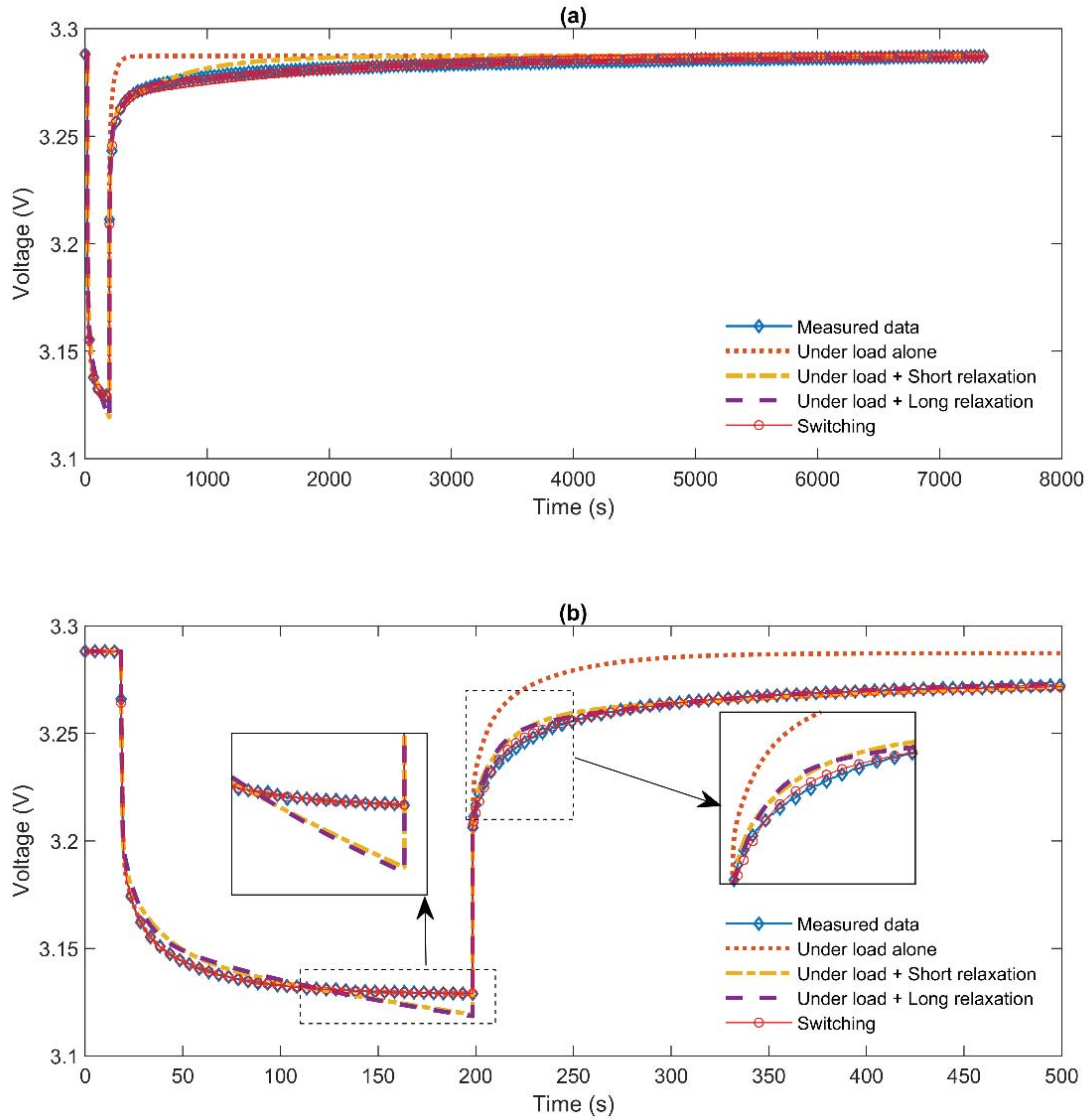
Figure 5: Test data and simulation results for the constant current discharge pulse experiment at 20°C thermal chamber ambient temperature, SoC starts at 50%, ends at 45%. (a) Comparison between the measured data with simulation results using 1. Underload time constant 2. Underload + short relaxation (500 seconds) time constant 3. Underload + long relaxation (7200 seconds) time constant, (b) Zoomed look for (a).

Data Selected/ Tau No.	Time constant 1/s	Time constant 2/s	Time constant 3/s
Case 1: Underload alone	0.21	6.4	35.7
Case 2: Underload + 500s relaxation	2.0	17.9	498.4
Case 3: Underload + 7200s relaxation	10.7	170.0	2285.1
Case 4: Switching Taus	Underload: 0.2 Relaxation: 1653	Underload: 6.4 Relaxation: 68.7	Underload: 35.7 Relaxation: 9.3

Table 1: Time constant used for the simulation results shown in Figure 5.

4.2. ECM parameter identification:

This section presents the full parameter identification procedure. The proposed method consists of two steps. The first step uses the underload test data to identify the underload RC time constants and the resistors values. The second step identifies the relaxation time constants using the relaxation region test data.

To reduce the complexity of the parameter optimization, the time constants of the RC networks are fixed throughout the entire SoC range and at various temperature levels. In this way, the resistor values become linear-in-the-variable parameters and can be solved using computationally efficient least squares tools. In literature, it is concluded by Hu et al. that the time constants of the RC networks can be considered as independent from SoC values. The benefit of this assumption is reducing the parameter identification complexity by finding the global minima of fewer parameters. The insensitivity of the variation of the capacitor values to the ECM-based SoC estimation accuracy further supports this assumption. [49] The RC time constants represent the time scale of interest for the voltage profile which can be considered independent from the working condition. The modelling results later show that this simplification doesn't lead to poor model accuracy.

4.2.1. Step 1: identification of the underload time constants and resistors

For a given set of the underload RC time constants, $\tau_{j,u}, j = 1,2,3$, the current passing through R_j (i.e., i_j) can be calculated in Eq (1). Denote $i_0 = i$ to represent the current passing through R_0 (to be consistent with $i_j, j = 1,2,3$).

To capture the SoC dependency of the resistor values, the full SoC operating window is divided using breakpoints as follows,

$$0 < SoC_1 < SoC_2 < \ldots < SoC_{n_{soc}} < 100\% \tag{5}$$

where n_{soc} is the number of SoC breakpoints. Next, define the triangle base function at each SoC breakpoint as follows,

$$f_1(SoC) = \begin{cases} 1, & if\ SoC < SoC_1 \\ \dfrac{SoC_2 - SoC}{SoC_2 - SoC_1}, & if\ SoC_1 \leq SoC < SoC_2 \end{cases}'$$

$$f_m(SoC) = \begin{cases} \frac{SoC - SoC_{m-1}}{SoC_m - SoC_{m-1}}, & if\ SoC_{m-1} \leq SoC < SoC_m \\ \frac{SoC_{m+1} - SoC}{SoC_{m+1} - SoC_m}, & if\ SoC_m \leq SoC < SoC_{m+1} \end{cases}, \quad m = 2, \dots, n_{soc} - 1 \quad (6)$$

$$f_{n_{soc}}(SoC) = \begin{cases} \frac{SoC - SoC_{n_{soc}-1}}{SoC_{n_{soc}} - SoC_{n_{soc}-1}}, & if\ SoC_{n_{soc}-1} \leq SoC < SoC_{n_{soc}} \\ 1, & if\ SoC_{n_{soc}} \leq SoC \end{cases}$$

The SoC dependency of the resistor values can now be expressed using linear interpolation as follows,

$$R_j = \sum_{m=1}^{n_{soc}} R_{j,m} f_m, \quad j = 0,1,2,3 \quad (7)$$

Then from the terminal voltage in Eq (3), yielding,

$$v - OCV = \sum_{j=0}^{n_{rc}} \left(\sum_{m=1}^{n_{soc}} R_{j,m} f_m \right) i_j \quad (8)$$

Here the time step indicator (k) is dropped from the variables, e.g., $v(k)$. Denote $y = v - OCV$, and row vector $F = [f_1, f_2, \dots, f_{n_{soc}}]$. Let row vector $p = [Fi_0, Fi_1, Fi_2, Fi_3]$ and $\theta = [R_{0,1}, R_{0,2}, \dots, R_{0,n_{soc}}, \dots, R_{3,1}, R_{3,2}, \dots, R_{3,n_{soc}}]$ as the collection of all the resistor values. Eq (8) can then be reformulated as

$$y = p\theta$$

Denote the value of y and p at time k as $y(k)$ and $p(k)$, respectively, and let

$$Y = \begin{bmatrix} y(1) \\ y(2) \\ \dots \\ y(N) \end{bmatrix}, P = \begin{bmatrix} p(1) \\ p(2) \\ \dots \\ p(N) \end{bmatrix}$$

Then from Eq (8) we obtain a least-squares formulation as follows,

$$Y = P\theta \quad (9)$$

Repeat the above procedure from Eq (5) to Eq(9) at the four different temperatures, and denote the Y, P and θ at $[10, 20, 30, 40]°C$ as $Y_{10}, Y_{20}, Y_{30}, Y_{40}$; $P_{10}, P_{20}, P_{30}, P_{40}$ and $\theta_{10}, \theta_{20}, \theta_{30}, \theta_{40}$ respectively.

Denote $P_s = blkdiag(P_{10}, P_{20}, P_{30}, P_{40})$ where '$blkdiag$' stands for block diagonal, $Y_s = [Y_{10}^T, Y_{20}^T, Y_{30}^T, Y_{40}^T]^T$ and $\theta_s = [\theta_{10}^T, \theta_{20}^T, \theta_{30}^T, \theta_{40}^T]^T$.

Then

$$Y_s = P_s \theta_s \tag{10}$$

The parameter constraints can be put as $\theta_{10} \geq \theta_{20} \geq \theta_{30} \geq \theta_{40}$ in elementwise. This comes from the prior knowledge that the resistance value decreases with temperature rise.

The optimal parameters to Eq (10), $\hat{\theta}_s$ can be obtained using least-squares solvers (here Matlab function 'lsqlin' is used). This is a convex optimization problem which can be solved efficiently. Then optimal resistor values can be calculated using the least squares method,

$$E_s = Y_s - P_s \hat{\theta}_s \tag{11}$$

and the modelling RMSE is $\sqrt{\frac{1}{N_s} E_s^T E_s}$, where N_s is the length of Y_s. Note that this RMSE depends on the choices of the underload RC time constants, $\tau_{j,u}$. Then the optimal $\tau_{j,u}$ can be obtained by solving the following parameter optimization problem

$$\min_{\tau_{1,u}, \tau_{2,u}, \tau_{3,u}} \sqrt{\frac{1}{N_s} E_s^T E_s} \tag{12}$$

Here, with only three parameters to optimize, the chance of finding the global minimum is greatly increased compared with optimizing all the model parameters together using the Genetic algorithm [50]. The Matlab function 'fminbnd' is used in this paper for finding the optimal underload RC time constants in Eq (12).

4.2.2. Step 2: identification of the relaxation time constants

Note that in Section 4.3.1, only the underload test data are used. Next, the rest relaxation test data will be used for identification of the relaxation RC time constants.

First, the underload time constants and the resistor values obtained in Section 4.3.1 are used to simulate the current values $i_j, j = 1,2,3$ under current load. Next, given

the relaxation time constants $(\tau_{1,r}, \tau_{2,r}, \tau_{3,r})$, the model's voltage profile during relaxation stage can be simulated using Eq (1) and Eq (3).

The model voltage during the relaxation stage will be compared with the measurements and the RMSE depends on the chosen relaxation time constants. This is an optimization problem similar to Eq (12). Again, with only three parameters $(\tau_{1,r}, \tau_{2,r}, \tau_{3,r})$ to optimize, the chance of finding the global minimum is high. The Matlab function 'fmincon' is used again for parameter optimization.

4.2.3.   Comparison against PIM without parameter switching scheme

In order to compare with the case that doesn't consider the load dependency of the ECM parameters, another PIM is given here that uses the same RC time constants for both underload and relaxation stages. The PIM with no switching consists of only the optimization step in Section 4.3.1 but uses different test data for parameter identification, i.e., both the underload and 2-hour relaxation test data are used for extracting the ECM parameters.

5. Modelling results vs validation results

In order to conduct a comparative study of the conventional PIM and the proposed PIM with switching, the model training results for the pulse discharge tests and 2 sets of validation tests are demonstrated in this section.

5.1. Model training results

The Figure 6 shows the model parameter training results for the two PIMs. Both PIMs perform under certain error bias within 20mV besides a few error spikes when the current jumps. In general, the PIM with no switching leads to better model accuracy during the relaxation stage and lower underload accuracy compared with the switching PIM, as it shows in Figure 6 (c) & (d). It is noticeable that the model accuracy decreases under low SoC (<5%).   Essentially, the training results show the overall RMSE errors are comparable, 2.4 mV and 3.4 mV for no switching and switching respectively. However, the underload phase RMSE errors are 7.1 mV and 1.8 mV for no switching and switching respectively, which demonstrates the benefits of using the switching PIM in this study. Figure 6 (c) & (d) shows a detailed investigation at SoC value of 85 % - 84%, where the cell underwent constant current

discharge for 180s (5% SoC breakpoint step) followed by a 2-hour relaxation. The PIM with no switching illustrates a better performance on the relaxation phase but poorer fitting on the underload phase, by contrast to the switching PIM as detailed in Figure 6 (c) & (d).

In Figure 6 (b) subplot, PIM with no switching delivers a noticeable large error spike at SoC value of 90%, where the underload time for the constant current period changes from 36s (1% SoC breakpoint step) to 180s (5% SoC breakpoint step). The larger error generated from PIM with no switching (maximum error about 21 mV) compares to switching PIM (maximum error about 8mV) shows another advantage of the proposed switching PIM. As the underload phase and the relaxation phase are trained individually, therefore the RC networks values have greater potential to overcome current load fluctuation during characterisation tests, which fits the potential needs for various current load characterisation tests.
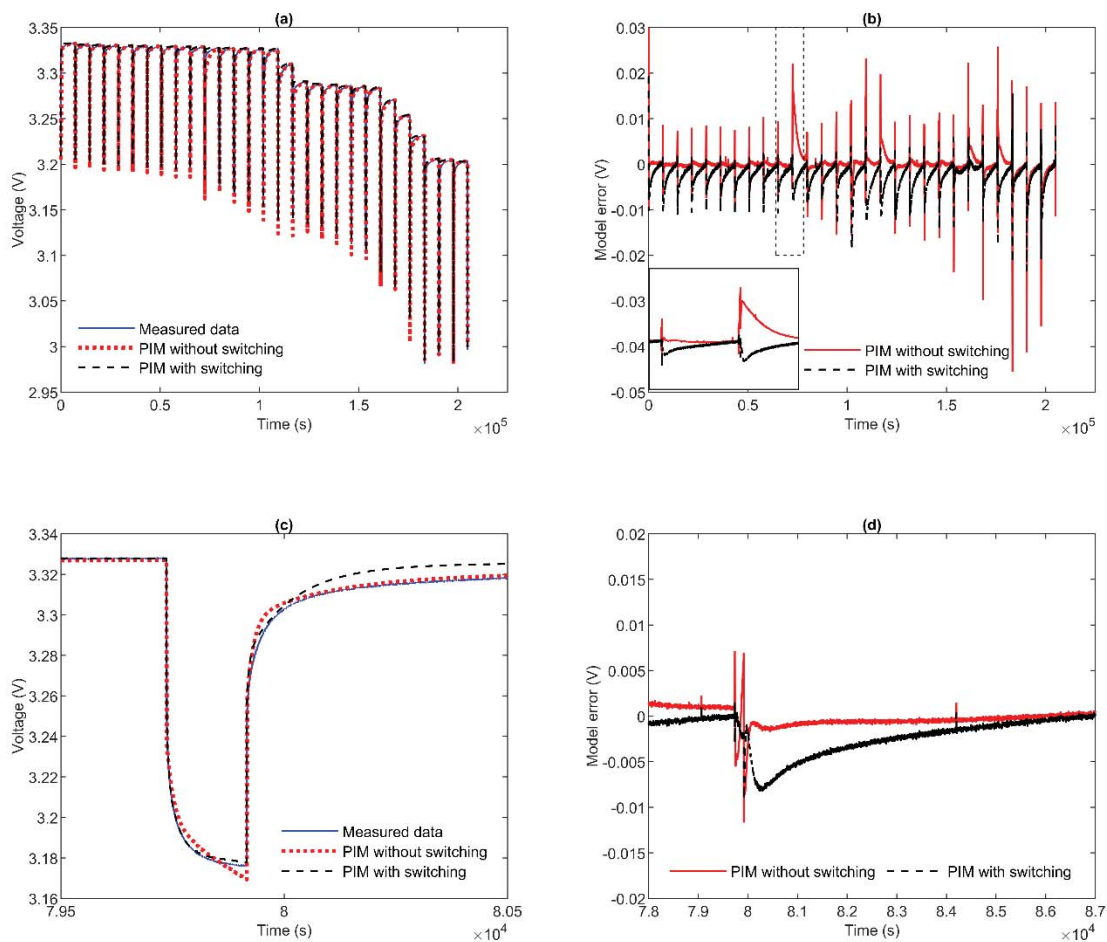

Figure 6 Comparison of the two PIM methods using the 1% & 5% SoC pulse discharge data at 1C (90A) with a 120minutes relaxation period at 20 °C (a): battery voltage fitting results, (b) modelling error & a zoomed segment

of the fitting error at SoC range 89% - 85%, (c): a zoomed segment of the battery voltage fitting results at SoC range 85% - 84%, (d) a zoomed segment of the modelling error at SoC range 85% - 84%.

5.2. Validation results:

In this study, there are 2 set of validation tests examined for both PIMs, which are constant current load and drive cycle noisy load. Normally if a set of parameters are trained from conventional PIM with pulse load as characterisation tests, then validation against constant current test data is typically not done, in many cases this is described as out of scope but is more likely because of poor agreement. Here, the proposed switching PIM is validated against both constant current and under load experimental data, to show its ability to reproduce a wide range of current loads.

5.2.1.   Constant Current load validation

Figure 7 (a) demonstrates the measured data together with simulated model results using both PIMs for a constant current discharge test at 1C (90A). The cell centre surface temperature acts as an additional input to the model. Figure 7 (b) demonstrates the error of both PIMs in voltage response. The overall modelling RMSE errors are 140.8 mV and 17.4 mV for PIM with no switching and switching PIM , respectively. The PIM with no switching shows a poor alignment between measured data and model simulation, where a constant error bias over 130 mV is observed. Meanwhile, the switching PIM delivers a good fit between measured data and simulation result. There is over 87.6% improvement on the error bias level from switching PIM.

This is because the PIM with no switching sacrifices partly the underload accuracy in order to improve the accuracy at the relaxation period, i.e., a trade-off. It is noteworthy that the model accuracy during the training step is acceptable, as shown in Figure 7. This problem of underload accuracy deficiency only becomes outstanding under this constant current discharge. In another word, the model training results can be misleading without careful data analysis. The root cause to this problem is that the battery shows distinctive dynamics properties for underload and relaxation. This effect must be taken into consideration during ECM parametrization and application.

It is therefore recommended that the training data set for ECM parametrization should have similar characteristics with the intended application of the model. In particular, if the intended application of the model includes constant current discharge, then a similar load profile should be used for ECM parametrization. This is a general recommendation for identifying a reduced order model from a highly complex or nonlinear system [46], which is however, generally overlooked in the ECM modelling field. The proposed PIM method using the parameter switching scheme effectively avoids this trade-off which would otherwise reduce the model underload accuracy.

There are similar features at low SoC region (<10%), where error is accumulated. This may be caused by the severe nonlinearity of the battery dynamics at this low SoC range, making constant-parameter ECM unsuitable for capturing the voltage profiles under different current profiles. The model accuracy at low SoC could be improved by taking into consideration of the difference between the surface and bulk concentrations of the battery electrode [51]. This, however, uses a different model structure from ECM and increases the model parametrization complexity. The low SoC accuracy of the ECM modelling will be explored in future work, however this is out of the scope for this study.
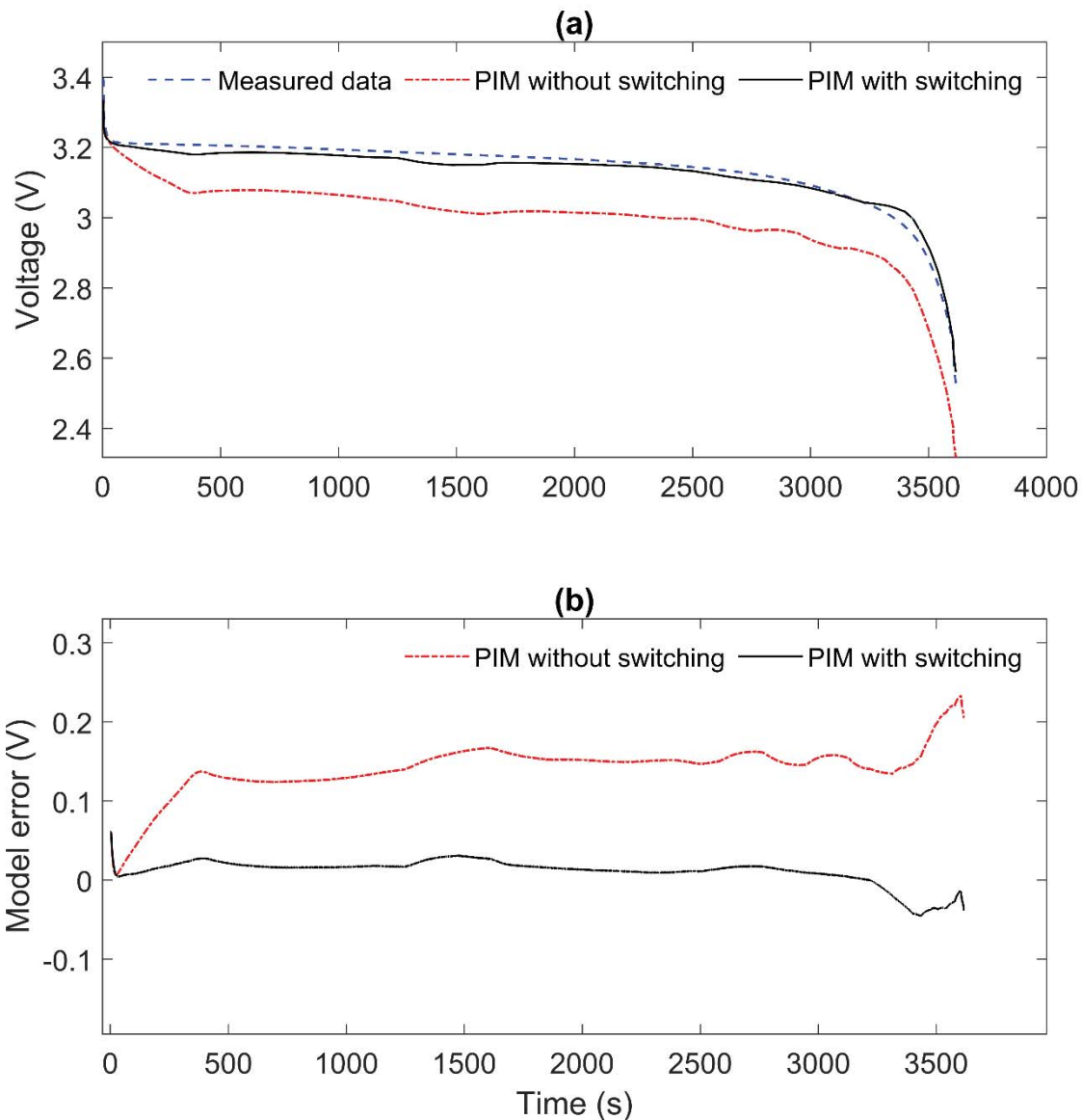
Figure 7 Comparison of the two PIM methods using the Constant Current discharge load at 1C (at 20 °C as starting thermal chamber ambient, cell centre temperature data is considered as an input for model simulation, (a): battery voltage fitting results; (b) modelling error

5.2.2. Drive cycle validation

A bespoke designed drive cycle based on a US06 drive cycle is subjected to the cell, where the input current is shown in Figure 3a. Figure 8 (a) demonstrates the measured data together with simulated model results using both PIMs. The cell centre surface temperature acts as an additional input to the model. Figure 8 (b) demonstrates the error of both PIMs in voltage response. The modelling overall RMSE errors are 78.2 mV and 17.7 mV for PIM with no switching and switching PIM, respectively. Also, the underload phase RMSE errors are 81.4 mV for PIM with no switching and 7.7 mV for switching PIM, where the switching PIM delivers 10 times less error (improved

90.5% for underload phase, and 77.4% for overall simulation) in this validation scenario. It is clear to see a constant error bias level about 75mV for the results generated from PIM with no switching, while the switching PIM offers an error bias level less than 10mV. The less error and more accurate model performance that uses the parameters generated from switching PIM proves the necessity of this PIM, especially for this type of battery. The reason for the difference of the model accuracy is similar to that in Figure 7.

All the PIMs trained the parameters across the entire SoC bandwidth together with 4 characterisation test temperatures. As shown in Figure 3 (c) and 4 (b), the cell centre surface temperature grows from 20 °C to 26 °C for drive cycle test and 20 °C to 35 °C, respectively. Training all the data together gives the model a smooth transition on these thermally dynamic scenarios.
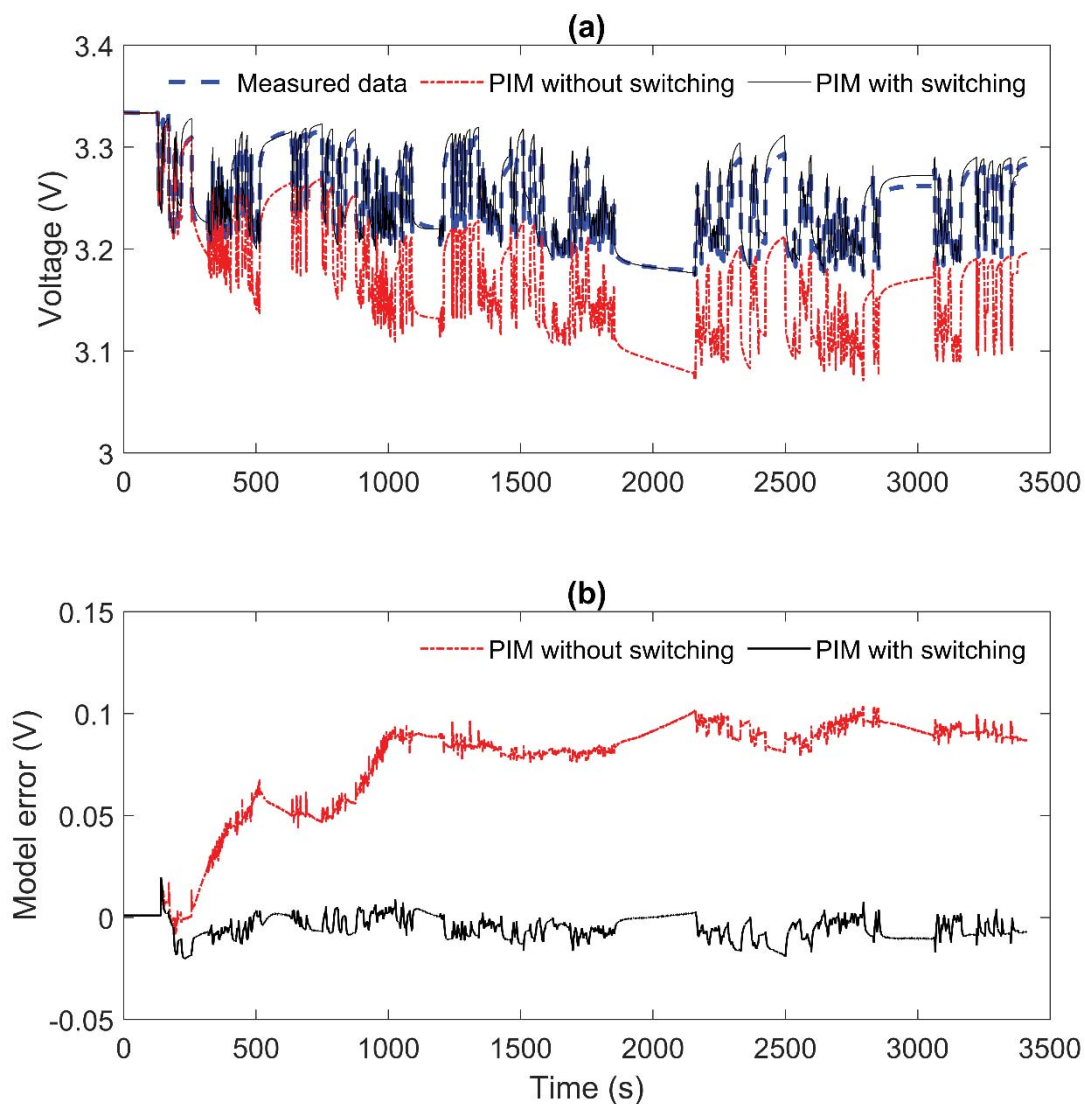
Figure 8 Comparison of the two PIM methods using the Drive cycle discharge load (input current is shown in Figure 3(a)) at 20 °C as starting thermal chamber ambient, cell centre temperature data is considered as an input for model simulation, (a): battery voltage fitting results; (b) modelling error

6. Conclusion and future work

A novel modified equivalent circuit model and parameter identification method is presented which takes into account the fact that many lithium ion batteries exhibit different time constants during underload operation compared to relaxation. The model switches between RC values for different current profiles. This is particularly pronounced in the large prismatic with lithium iron phosphate cathode studied in this paper but is also seen at the extremes of SOC in other lithium ion batteries, particularly at low SOC where state estimation can be particularly difficult yet even more important. The approach presented in this paper demonstrates significant improvements over a conventional equivalent circuit model without switching time constants. The work should be of interest to application engineers, battery management system developers, and control engineers.

The study in this paper is limited to the specific phenomena of the battery's different dynamics between underload and relaxation. The discharge current pulses are used for model training and parameter identification, and the model performance is validated under constant-current full discharge and drive cycle profile. A more detailed analysis of the ECM's parameter dependency on the load current profile (such as frequency spectrum of the drive cycles) and the corresponding parameter-switching scheme are left for future work. Further, although frequency domain methods such as Fourier

transform have been widely used for input profile characterization and categorization, a time domain method for the classification of current profile still needs to be developed and validated for real-time BMS implementation.

7. Supplementary material

Figure 1-3: Model training results for other temperatures + experimental data for other temperatures

Figure 4-6: CC discharge validation for other temperatures + experimental data for other temperatures

Figure 7: OCV curves for different temperatures

Figure 8: The identified model parameters – resistor values versus SoC and temperature

Figure 9: ECM model structure with n RC networks

Table 1. The identified underload and relaxation RC time constants of the ECM

8. Acknowledge

References

[1]   Wikipedia, Phase-out of fossil fuel vehicles, 2020.

[2]   H.Y. He Kebin, Zhang Qiang, Ming Dengli , Wu Ye , Catherine Witherspoon, Valentin Foltescu, Q.Y. , Cheng Jing, A Review of 20 years' Air Pollution Control in Beijing, Nairobi, Kenya, 2019.

[3]   C. Mckerracher, Electric Vehicle Outlook 2019, 2019.

[4]   S. Yan, S. Luo, J. Feng, P. Li, R. Guo, Q. Wang, Y. Zhang, Y. Liu, S. Bao, Rational design of flower-like FeCo2S4/reduced graphene oxide films: Novel binder-free electrodes with ultra-high conductivity flexible substrate for high-performance all-solid-state pseudocapacitor, Chem. Eng. J. 381 (2020) 122695. https://doi.org/https://doi.org/10.1016/j.cej.2019.122695.

[5]   S. Luo, D. Hu, H. Liu, J. Li, T.-F. Yi, Hydrothermal synthesis and characterization of α-Fe2O3/C using acid-pickled iron oxide red for Li-ion batteries, J. Hazard. Mater. 368 (2019) 714–721.

https://doi.org/https://doi.org/10.1016/j.jhazmat.2019.01.106.

[6]   L. Lu, X. Han, J. Li, J. Hua, M. Ouyang, A review on the key issues for lithium-ion battery management in electric vehicles, J. Power Sources. 226 (2013) 272–288.

[7]   A. Seaman, T.-S. Dao, J.L.B. circuit model McPhee   electrochemical model, reduced order model, parameter sensitivity analysis, -- good reference papers, J. McPhee,   parameter sensitivity analysis – good reference papers J.L.B.- equivalent circuit model McPhee   electrochemical model reduced order model, J. McPhee,   parameter sensitivity analysis – good reference papers J.L.B.- equivalent circuit model McPhee   electrochemical model reduced order model, J. McPhee, A survey of mathematics-based equivalent-circuit and electrochemical battery models for hybrid and electric vehicle simulation, J. Power Sources. 256 (2014) 410–423.

[8]   E. Chemali, P.J. Kollmeyer, M. Preindl, A. Emadi, State-of-charge estimation of Li-ion batteries using deep neural networks: A machine learning approach, J. Power Sources. 400 (2018) 242–255.

[9]   V. Klass, M. Behm, G. Lindbergh, Capturing lithium-ion battery dynamics with support vector machine-based battery model, J. Power Sources. 298 (2015) 92–101. https://doi.org/https://doi.org/10.1016/j.jpowsour.2015.08.036.

[10]   M. Doyle, J. Newman, The use of mathematical modeling in the design of lithium/polymer battery systems, Electrochim. Acta. 40 (1995) 2191–2196. https://doi.org/10.1016/0013-4686(95)00162-8.

[11]   M. Doyle, Modeling of Galvanostatic Charge and Discharge of the Lithium/Polymer/Insertion Cell, J. Electrochem. Soc. 140 (1993) 1526. https://doi.org/10.1149/1.2221597.

[12]   R. Darling, Modeling a Porous Intercalation Electrode with Two Characteristic Particle Sizes, J. Electrochem. Soc. 144 (1997) 4201. https://doi.org/10.1149/1.1838166.

[13]   P. Ramadass, B. Haran, R. White, B.N. Popov, Mathematical modeling of the capacity fade of Li-ion cells, J. Power Sources. 123 (2003) 230–240.

https://doi.org/10.1016/S0378-7753(03)00531-7.

[14] R. Klein, N.A. Chaturvedi, J. Christensen, J. Ahmed, R. Findeisen, A. Kojic, Electrochemical model based observer design for a lithium-ion battery, IEEE Trans. Control Syst. Technol. (2013). https://doi.org/10.1109/TCST.2011.2178604.

[15] D.E. Stephenson, E.M. Hartman, J.N. Harb, D.R. Wheeler, Modeling of Particle-Particle Interactions in Porous Cathodes for Lithium-Ion Batteries, J. Electrochem. Soc. 154 (2007) A1146. https://doi.org/10.1149/1.2783772.

[16] M. Guo, G.-H. Kim, R.E. White, A three-dimensional multi-physics model for a Li-ion battery, J. Power Sources. 240 (2013) 80–94. https://doi.org/10.1016/j.jpowsour.2013.03.170.

[17] Y. Merla, B. Wu, V. Yufit, R.F. Martinez-Botas, G.J. Offer, An easy-to-parameterise physics-informed battery model and its application towards lithium-ion battery cell design, diagnosis, and degradation, J. Power Sources. 384 (2018) 66–79. https://doi.org/10.1016/j.jpowsour.2018.02.065.

[18] P.W.C. Northrop, V. Ramadesigan, S. De, V.R. Subramanian, Coordinate Transformation, Orthogonal Collocation, Model Reformulation and Simulation of Electrochemical-Thermal Behavior of Lithium-Ion Battery Stacks, J. Electrochem. Soc. 158 (2011) A1461. https://doi.org/10.1149/2.058112jes.

[19] M. Ecker, T.K.D. Tran, P. Dechent, S. Käbitz, A. Warnecke, D.U. Sauer, Parameterization of a physico-chemical model of a lithium-ion battery i. determination of parameters, J. Electrochem. Soc. 162 (2015) A1836–A1848.

[20] E. Prada, D. Di Domenico, Y. Creff, J. Bernard, V. Sauvant-Moynot, F. Huet, Simplified Electrochemical and Thermal Model of LiFePO 4 -Graphite Li-Ion Batteries for Fast Charge Applications, J. Electrochem. Soc. 159 (2012). https://doi.org/10.1149/2.064209jes.

[21] Y. Zhao, Y. Patel, T. Zhang, G.J. Offer, Modeling the effects of thermal gradients induced by Tab and surface cooling on Lithium ion cell performance, J. Electrochem. Soc. 165 (2018) A3169–A3178.

[22] M. Guo, R.E. White, A distributed thermal model for a Li-ion electrode plate

pair, J. Power Sources. 221 (2013) 334–344. https://doi.org/10.1016/j.jpowsour.2012.08.012.

[23]   B. Pattipati, C. Sankavaram, K.R. Pattipati, System identification and estimation framework for pivotal automotive battery management system characteristics, IEEE Trans. Syst. Man Cybern. Part C Appl. Rev. (2011). https://doi.org/10.1109/TSMCC.2010.2089979.

[24]   H. He, R. Xiong, H. Guo, S. Li, Comparison study on the battery models used for the energy management of batteries in electric vehicles, Energy Convers. Manag. 64 (2012) 113–121.

[25]   X. Hu, S. Li, H. Peng, A comparative study of equivalent circuit models for Li-ion batteries, J. Power Sources. 198 (2012) 359–367.

[26]   W. Allafi, K. Uddin, C. Zhang, R.M.R.A. Sha, J. Marco, On-line scheme for parameter estimation of nonlinear lithium ion battery equivalent circuit models using the simplified refined instrumental variable method for a modified Wiener continuous-time model, Appl. Energy. 204 (2017) 497–508.

[27]   A. Barai, W.D. Widanage, J. Marco, A. McGordon, P. Jennings, A study of the open circuit voltage characterization technique and hysteresis assessment of lithium-ion cells, J. Power Sources. 295 (2015) 99–107.

[28]   C. Zhang, W. Allafi, Q. Dinh, P. Ascencio, J. Marco, Online estimation of battery equivalent circuit model parameters and state of charge using decoupled least squares technique, Energy. 142 (2018) 678–688.

[29]   C. Zhang, K. Li, J. Deng, S. Song, Improved Realtime State-of-Charge Estimation of LiFePO4 Battery Based on a Novel Thermoelectric Model, IEEE Trans. Ind. Electron. 64 (2017) 654–663.

[30]   H. He, R. Xiong, J. Fan, Evaluation of Lithium-Ion Battery Equivalent Circuit Models for State of Charge Estimation by an Experimental Approach, Energies . 4 (2011). https://doi.org/10.3390/en4040582.

[31]   W. Gao, Y. Zheng, M. Ouyang, J. Li, X. Lai, X. Hu, Micro-short-circuit diagnosis for series-connected lithium-ion battery packs using mean-difference model, IEEE Trans. Ind. Electron. (2019).

https://doi.org/10.1109/TIE.2018.2838109.

[32] H. Dai, T. Xu, L. Zhu, X. Wei, Z. Sun, Adaptive model parameter identification for large capacity Li-ion batteries on separated time scales, Appl. Energy. 184 (2016) 119–131.

[33] K.C. Lim, H.A. Bastawrous, V.H. Duong, K.W. See, P. Zhang, S.X. Dou, Fading Kalman filter-based real-time state of charge estimation in LiFePO4 battery-powered electric vehicles, Appl. Energy. 169 (2016) 40–48. https://doi.org/10.1016/j.apenergy.2016.01.096.

[34] X. Lai, W. Gao, Y. Zheng, M. Ouyang, J. Li, X. Han, L. Zhou, A comparative study of global optimization methods for parameter identification of different equivalent circuit models for Li-ion batteries, Electrochim. Acta. 295 (2019) 1057–1066.

[35] W.D. Widanage, A. Barai, G.H. Chouchelamane, K. Uddin, A. McGordon, J. Marco, P. Jennings, Design and use of multisine signals for Li-ion battery equivalent circuit modelling. Part 2: Model estimation, J. Power Sources. 324 (2016) 61–69.

[36] C. Zhang, K. Li, L. Pei, C. Zhu, An integrated approach for real-time model-based state-of-charge estimation of lithium-ion batteries, J. Power Sources. 283 (2015) 24–36.

[37] S. Thanagasundram, R. Arunachala, K. Makinejad, T. Teutsch, A. Jossen, A cell level model for battery simulation, in: Eur. Electr. Veh. Congr., 2012: pp. 1–13.

[38] M. Verbrugge, B. Koch, Generalized recursive algorithm for adaptive multiparameter regression application to lead acid, nickel metal hydride, and lithium-ion batteries, J. Electrochem. Soc. 153 (2006) A187–A201.

[39] C. Campestrini, M.F. Horsche, I. Zilberman, T. Heil, T. Zimmermann, A. Jossen, Validation and benchmark methods for battery management system functionalities: State of charge estimation algorithms, J. Energy Storage. 7 (2016) 38–51.

[40] M. Ceraolo, J. Gazzarri, R. Jackey, P. Sanghvi, M. Saginaw, T. Huria, Battery

Model Parameter Estimation Using a Layered Technique: An Example Using a Lithium Iron Phosphate Cell, SAE Tech. Pap. Ser. 1 (2013). https://doi.org/10.4271/2013-01-1547.

[41]   H.P.G.J. Beelen, H.J. Bergveld, M.C.F. Donkers, On Experiment Design for Parameter Estimation of Equivalent-Circuit Battery Models, in: 2018 IEEE Conf. Control Technol. Appl., 2018: pp. 1526–1531. https://doi.org/10.1109/CCTA.2018.8511529.

[42]   X. Tang, F. Gao, C. Zou, K. Yao, W. Hu, T. Wik, Load-responsive model switching estimation for state of charge of lithium-ion batteries, Appl. Energy. 238 (2019) 423–434.

[43]   M. Lenz, D. Jöst, F. Thiel, S. Pischinger, D.U. Sauer, Identification of load dependent cell voltage model parameters from sparse input data using the Mixed Integer Distributed Ant Colony Optimization solver, J. Power Sources. 437 (2019) 226880. https://doi.org/https://doi.org/10.1016/j.jpowsour.2019.226880.

[44]   J. Brand, Z. Zhang, R.K. Agarwal, Extraction of battery parameters of the equivalent circuit model using a multi-objective genetic algorithm, J. Power Sources. 247 (2014) 729–737.

[45]   S.K. Rahimian, S. Rayman, R.E. White, Comparison of single particle and equivalent circuit analog models for a lithium-ion cell, J. Power Sources. 196 (2011) 8450–8462.

[46]   J. Schoukens, L. Ljung, Nonlinear System Identification: A User-Oriented Roadmap, ArXiv Prepr. ArXiv1902.00683. (2019).

[47]   W. Waag, S. Käbitz, D.U. Sauer, Application-specific parameterization of reduced order equivalent circuit battery models for improved accuracy at dynamic load, Measurement. 46 (2013) 4085–4093. https://doi.org/https://doi.org/10.1016/j.measurement.2013.07.025.

[48]   G.L. Plett, Extended Kalman filtering for battery management systems of LiPB-based HEV battery packs: Part 2. Modeling and identification, J. Power Sources. 134 (2004) 1369–1384.

https://doi.org/https://doi.org/10.1016/j.jpowsour.2004.02.032.

[49]   C. Zhang, L.Y. Wang, X. Li, W. Chen, G.G. Yin, J. Jiang, Robust and
       Adaptive Estimation of State of Charge for Lithium-Ion Batteries, IEEE Trans.
       Ind. Electron. 62 (2015) 4948–4957.
       https://doi.org/10.1109/TIE.2015.2403796.

[50]   A. Malik, Z. Zhang, R.K. Agarwal, Extraction of battery parameters using a
       multi-objective genetic algorithm with a non-linear circuit model, J. Power
       Sources. 259 (2014) 76–86.
       https://doi.org/https://doi.org/10.1016/j.jpowsour.2014.02.062.

[51]   M. Ouyang, G. Liu, L. Lu, J. Li, X. Han, Enhancing the estimation accuracy in
       low state-of-charge area: A novel onboard battery model through surface state
       of charge determination, J. Power Sources. 270 (2014) 221–237.